Microstructure evolution and properties of gradient nanostructures subjected to laser shock processing in 300M ultra-high strength steel

Yun-fei Ma[a], Yi Xiong[a,b*], Zheng-ge Chen[c], Xiao-qin Zha[d], Tian-tian He[a], Yong Li[e] ,

Harishchandra Singh[f], Jukka Kömi[g], Marko Huttula[a,f], Wei Cao[f]

[a] *School of Materials Science and Engineering, Henan University of Science and Technology, Luoyang 471023, China*

[b] *Collaborative Innovation Center of Nonferrous Metals, Luoyang 471023, China*

[c] *State Key Laboratory of Laser Interaction with Matter, Northwest Institute of Nuclear Technology, Xi'an 710024, China*

[d] *Luoyang Ship Material Research Institute, Luoyang 471000, China*

[e] *Central Iron and Steel Research Institute, Beijing 100081, China*

[f] *Nano and Molecular Systems Research Unit, University of Oulu, FIN-90014, Finland*

[g] *Materials and Mechanical Engineering, Center for Advanced Steels Research, University of Oulu, FIN-90014, Finland*

Abstract

Gradient nanostructures (GNs) were created in 300M ultra-high strength (UHS) steel by laser shock processing (LSP). Microstructure evolution and properties of GNs subjected to LSP with different pulse energies were thoroughly characterized on 3D profiler, scanning electron microscope (SEM), transmission electron microscope (TEM), X-ray diffractometer (XRD), X-ray stress analyzer, nano-indenter and tensile tester. Results showed successful creations of GNs in 300M steel after LSP treatments. With the increase in pulse energy, the size of the surface layer was refined from 15 nm (3J) to 10 nm (7J), and the corresponding grains were amorphized to some extent. Meanwhile, many substructure defects such as dislocation tangles and deformation twins (DTs) were noted in the subsurface. The dislocation density and the number of DTs increased with the pulse energy. Further, the high compressive residual stress was

* Corresponding author.

E-mail address: xy_hbdy@163.com (Y. Xiong)

introduced to the 300M steel surface after LSP, and the corresponding hardness was improved substantially. The compressive residual stress, depth of the affected layer and the hardness rose significantly with the pulse energy. Beside improvements in strength and plasticity, the fracture morphology was changed from a typical ductile fracture to quasi-cleavage and ductile mixed fracture.

Keywords: 300M steel; Gradient nanostructures; Laser shock processing; Microstructure evolution; Mechanical properties

1. Introduction

Owing to the super high strength (≥ 1800 MPa) and excellent plastic toughness, 300M ultra-high strength (UHS) steel has become the key component in advanced aircraft landing gears [1-3]. However, due to complex alternating loads and strong impacts from the ground in service, the landing gear often suffers from micro-cracks, micro-fractures, unpredictable fatigue failures and even surface fractures [4, 5]. These unfavorable phenomena pose high risks to the overall safety of the aircrafts. A few studies demonstrate that the surface strengthening technology can effectively improve the properties of 300M steel against fatigue fracture, enhance the reliability and safety of the component, and prolong the service life.

In recent years, several researches were focused on improving mechanical properties of 300M steel through different surface treatments techniques. Bag et al. [6] studied the effect of surface shot peening (SP) on the growth of short cracks in 300M steel. It was found that the compressive residual stress induced by SP treatment effectively hindered growths of short cracks along with a decreased crack growth rate and increased fatigue life. Zhao et al. [7] reported the formation of a surface hardened layer on the treated surface of 300M steel by ultrasonic surface rolling processing (USRP). Increments in the compressive residual stress and surface hardness were observed while the surface roughness was decreased, which further resulted in a

significant increase in the fretting fatigue and corrosion fatigue performance of 300M steel. Liu et al. [8] employed an electric pulse-assisted ultrasonic nanocrystal surface modification (EP-UNSM) method to change the surface integrity of 300M steel. A plastically deformed layer was introduced on the sample surface. At the same time, dislocation tangles were noted in forms of dislocation walls and dislocation cells, which further refined grains and produced small number of twins. Surface hardness of the treated material was increased accordingly. Moreover, Liu et al. [9] studied the effect of laser-assisted ultrasonic nanocrystal surface modification (LA-UNSM) method towards microstructure and mechanical properties of 300M steel. In addition to the plastic deformation layer, surface hardness increases were attributed to the refinement of the lath martensite and formation of oxides. Favorable work-hardness effects were also observed after LA-UNSM treatment. From the above, these surface strengthening technologies are found useful to improve the microstructure and properties of 300M steel. Despite the progresses, the aforementioned technologies are flawed in the following aspects. For example, the traditional SP and USRP technologies can obtain shallow residual compressive stress fields and large surface roughness, and the surface is prone to form micro-cracks, which hinder the increase of material performance. Also, the UNSM method has the disadvantages of inefficient, practical difficulty and high cost, which altogether limits their implementation for mass production.

In fact, microstructure evolution of gradient nanostructures (GNs) of metallic materials subjected to severe plastic deformation (SPD) mainly depends on material characteristics, stacking fault energy (SFE), crystal structure and deformation mode [10]. Nanocrystals in materials with a body-centered cubic (BCC) structure and high SFE have shown that dislocation walls and dislocation tangles transformed into sub-grain boundaries (SGBs) via dislocation accumulation, rearrangement, and annihilation. Thereafter, SGBs absorbed the gliding dislocations and rotated, and then evolved into high-angle grain boundaries (HAGBs), which increased surface grain refinement [11]. In austenitic stainless 316L steel with a face-centered cubic (FCC)

structure and medium SFE, the microbands and shear bands of recrystallization and recrystallization twinning were widely formed, leading to grain sub-division [12]. However, for 304 stainless steel with a low SFE, the interaction of ultrafine twins resulted in grains refinement, and a phase transformation was also identified [13]. Besides, mechanical twinning was found in titanium samples [14] with an atypical hexagonal close-packed (HCP) crystal structure due to the presence of four independent slip systems. The twins and their crossovers rapidly reduced the scale of microstructure.

Laser shock processing (LSP) is a new and promising surface treatment technique which has been used to improve mechanical properties [15] and fatigue life [16] of metals and alloys. The generated shock wave can introduce deep compressive residual stresses of several hundreds of MPa by exposing metallic samples to high power density and short pulse laser beams. It has been reported to have many advantages such as controllable heating source, no thermal influence, significant strengthening effect and strong adaptability [17]. Wu [18] investigated LSP on 40CrNi2Si2MoVA steel with multiple pulses. It was found that increasing the shock times greatly raises the surface residual stress of the sample and the stress distribution is evener. Pistochini et al. [19] compared the fatigue performance generated by LSP and SP on 300M steel, it was found that LSP resulted in a large and deep compressive residual stress field, which significantly improved the fatigue strength and stress corrosion resistance of 300M steel. Such modifications prolonged the service life of the aircraft landing gear, and has great application prospect in military and civil aircraft manufacturing. However, previous researches are limited to the improvement of residual stress distribution and fatigue performance of 300M steel induced by LSP treatment. Microstructure evolution and properties of GNs subjected to LSP treatment were scarcely reported for UHS 300M steel treated by LSP under different pulse energies. In this work, we presented a systematic study of the microstructure evolution and properties of GNs induced by LSP in UHS 300M steel. By unveiling the effect of laser pulse energies on the microstructure evolution and properties of

UHS 300M steel, it is hoped to provide the feasible parameters of LSP to strengthen the service performance of 300M steel landing gears. This work is aimed to provide an experimental basis and technical support for the enhancement of aircraft landing gear surface structure and the application of the typical UHS 300M steel for key components by using the LSP technique, so as to achieve the goal of lightweight and reliable aircraft landing gear.

2. Materials and experimental procedures

The 300M steel (40CrNi2Si2MoVA) was used to engineer the investigated steel ingot with the chemical composition shown in Table 1. All specimens were annealed at 870 ℃ for 1 h followed by quenching in oil and then tempering at 300℃ for 2 h. They were air cooled while tempering twice. The mechanical properties of treated 300M steel are shown in Table 2, which clearly shows that 300M steel has the ultra-high strength and excellent ductility.

Table 1 Chemical composition of 300M steel (wt.%).

C	Cr	Mn	Si	Ni	Mo	V	Cu	Fe
0.42	0.85	0.82	1.57	1.94	0.38	0.09	0.84	Bal.

Table 2 Mechanical properties of 300M steel after heat treatment.

Tensile strength σ_b /MPa	Yield strength $\sigma_{0.2}$/MPa	Elongation δ/%	Reduction of area φ/%
1815	1511	11.8	52.9

Tensile test specimens of 300M steel were prepared by wire cutting, as shown in Fig. 1a. Subsequent LSP treatment was conducted on the gauge surface (4.5×30 mm)

of the sample, and the scanning path was parallel to the X-axis direction (Fig. 1b). The LSP experiments were performed using a YS 0805-R200A laser shock peening of Xi'an Tyrida Optical Electric Technology Co., Ltd. operated at 3 Hz with a wavelength of 1064 nm, and a pulse width (full width at half maximum, FWHM) of 20 ns. The laser pulse energies are 3J and 7J, respectively. Both sides of the samples were treated by 1 pass LSP. The spot diameter and the overlap rate were 3 mm and 50%, respectively. For LSP, the workpiece surface is first coated with an overlay opaque to laser beam and then covered with a transparent overlay. A water layer with a thickness of about 1~2 mm was used as the transparent confining layer to enhance the peak pressure induced by laser shock wave, and the black tape with a thickness of 120 μm was used as an absorbing layer to protect the sample surface from thermal effects. When the laser with short pulse and high peak power density irradiates the workpiece surface, the absorbing layer on the workpiece surface absorbs the laser energy and undergoes explosive vaporization and evaporation, generating a high-pressure plasma shock wave. By using the force effect of shock wave, the microstructure of surface material changes and the compressive residual stress produces at the deeper thickness, so as to improve the fatigue resistance performance of metal materials. The detailed processing parameters used in LSP are listed in Table 3.

Table 3 Processing parameters used in LSP treatment.

Parameter	Value
Output beam divergence/mrad	⩽2
Laser wavelength/nm	1064
Repetition rate/Hz	3
Pulse width/ns	20
Pulse energy/J	3 or 7

Spot diameter/mm	3
Overlapping rate/%	50
Pulse to pulse energy stability/%	＜1

After LSP treatments with different pulse energies, the surface roughness of the samples was characterized by a Nanovea HS1000P 3D profiler. Scanning electron microscopy (SEM, JSM-IT200) was employed for surface morphology analysis. Cross sections of the specimens were polished and then etched using 4% Nital solution for 3-5 s. The surface GNs of samples was measured by a JSM-IT200 SEM at an accelerating voltage of 20 KV. The specimens with a thickness of 0.5 mm were intercepted by wire cutting and mechanically thinned down to about 50 μm by using one-sided grinding of waterproof abrasive paper. The sheet of φ3 mm was pressed out in the mould and thinned on a Gatan 691 ion milling technique. A transmission electron microscopy (TEM, JEM-2010) was used to examine the surface and subsurface microstructure of the processed specimens, and the operating voltage of the TEM was 200 kV. D8 ADVANCE X-ray diffractometer (XRD) was used to study the crystal structure of LSP treated samples and the tube voltage was 40 kV. The tube anode was Cu Kα1 (λ=0.15406 nm), and the width of the receiving silt was 2 mm. The feed angle of the ladder scanning was 0.02° and the ranges from 40° to 100°. The residual stresses of the samples after LSP with different pulse energy were determined by using an X-350A XRD with $\sin^2\theta$ method. The X-ray beam diameter was about 4 mm. The diffraction plane was α phase (211) plane. The scanning starting angle and terminating angle were 152° and 160°, respectively. For the measurement of the residual stress along the depth direction, the electropolishing material removal method was used. Subsequently, hardness of the laser processed regions was measured by using G200 nanoindenter (500mN load, 5mN/s loading rate, 10s holding time). The mechanical properties were measured by Instron 5587 tensile tester with a speed of 0.5mm/min. The fracture of the tensile specimen was observed via JSM-IT200 SEM.

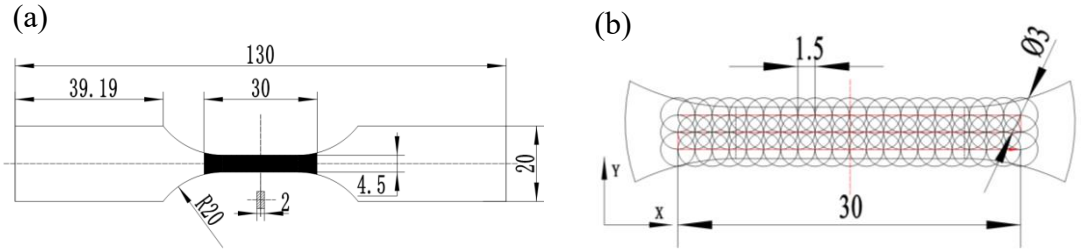

Fig. 1 (a) Dimension of tensile sample (b) Partial enlargement drawing of the treated area subjected to LSP (mm).

3. Results

3.1 Surface topography and roughness

Fig. 2 depicts SEM images of the surface morphologies and roughness of 300M steel after LSP treatments with different pulse energies. There are no obvious defects on the surface of the untreated sample, but strip-shaped scratches as a result of mechanical grinding. The noted surface roughness (Sa) is 1.27 μm and the peak-valley value (PV) is 6.53 μm, from Fig. 2a and 2b. After LSP, small micro-cracks appear on the surface of 300M steel and the depth of strip scratches became shallower. The values of Sa and PV are reduced to 0.86 μm and 3.51 μm, respectively, as shown in Fig. 2c and 2d. Due to the high laser density of 50% overlap rate of LSP, the space of the impact valleys formed on the surface of 300M steel becomes smaller and the scratches on the surface are extruded, resulting in observed decrease in Sa. Furthermore, the stress induced by the shock wave has a Gaussian distribution due to the character of the laser pulse energy [20]. The severe plastic deformation on the surface is uneven, leading to the stress concentration, which induces the initiation and propagation of cracks. Consequentially, some small micro-cracks are formed. With the increase of laser energy, the high energy shock wave exerts huge compressive stress on the surface of 300M steel, resulting in slight bending deformation on the surface of the sample (shown via circle in Fig. 2e), and the formation of micro-pits and wrinkles. As a result, Sa and PV slightly rose to 0.99 and 6.20 μm, respectively. Meanwhile, the intensification of stress concentration

promotes the initiation and propagation of cracks and causes the increase in length and number of micro-cracks on the surface of 300M steel (Fig. 2e and 2f). The surface roughness of 300M steel reduces after LSP treatment. This is also consistent with the results of LY2 Al alloys by multiple LSP impacts [21]. The surface quality of 300M steel is improved, which raises the fatigue resistance of the sample.

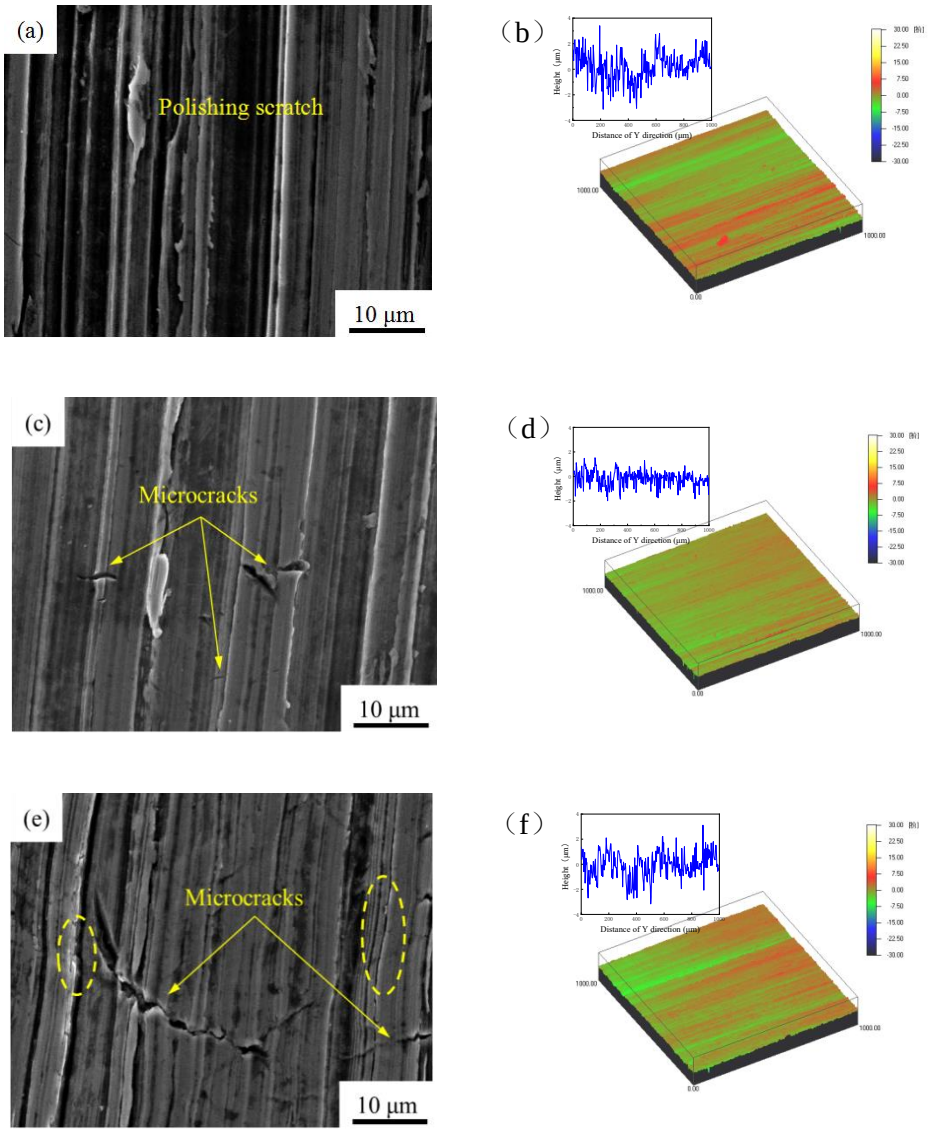

Fig. 2 Surface morphologies of 300M steel subjected to LSP with different pulse energies: (a, b) untreated; (c, d) LSP-3J; (e, f) LSP-7J.

3.2 Microstructure evolution

Fig. 3 shows the SEM images of 300M steel after LSP with different pulse energies. The interlaced acicular tempered martensite can be found in the untreated samples from Fig. 3a. During the LSP treatment, the impact energy was transformed into the deformation energy storage inside the material and the strain rate and strain on the surface of the sample became high. Thus, an SPD layer with the thickness of 9 μm is observed on the surface of 300M steel due to ultra-high strain rate (10^6~10^7 s^{-1}). With the increase in distance from the surface, the strain rate and strain reduced gradually, and the deformation degree declined, forming a minor plastic deformation (MPD) layer on the subsurface of the sample (see Fig. 3b). The plastic deformation layer formed on the surface of the sample after LSP is composed of the SPD layer and MPD layer. The depth of the SPD layer increased to about 18 μm as the pulse energy rised (Fig. 3c). Similar structures were observed in AISI 420 steel [22] and ANSI 304 steel [23] followed by LSP treatment. This is mainly because the deep compressive residual stress introduced by the generated shock wave is far beyond the dynamic yield strength of the material, which causes the severe plastic deformation on the surface of the sample. As the shock wave propagates into the material, the pressure gradually reduces, the deformation and strain rate also decrease, which causes the decrease of the deformation degree of the subsurface of the material [24].

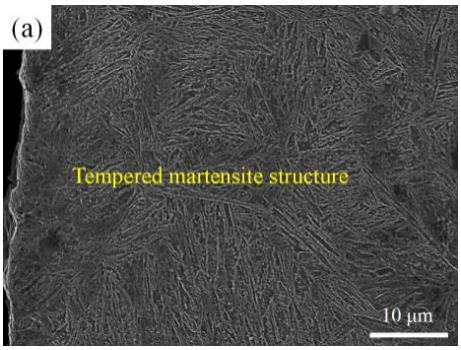

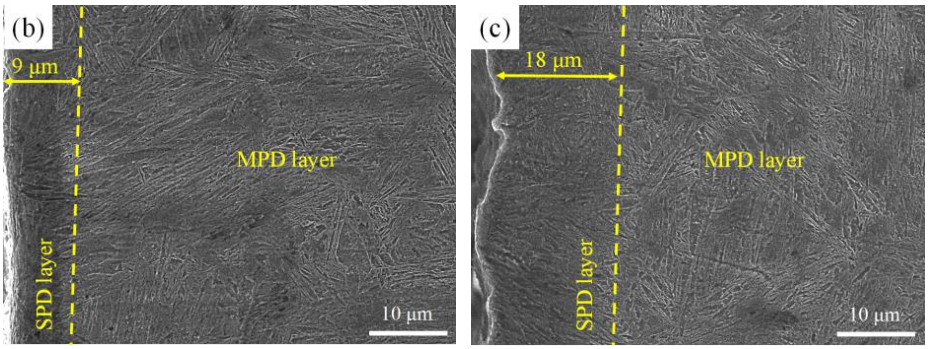

Fig. 3 SEM images of 300M steel subjected to LSP with different pulse energies: (a) untreated; (b) LSP-3J; (c) LSP-7J.

Fig. 4 shows TEM images of 300M steel surfaces after LSP with different laser pulse energies. After LSP with a low energy of 3J, high density dislocation tangles occur on the surface of 300M steel. The acicular tempered martensite is severely broken, which further refines grains, denoted in Fig. 4a and 4b. The selective area electron diffraction (SAED, Fig. 4a) pattern shows a clear and uniformly continuous diffraction ring pattern, which indicates that grains are refined to nano scale and grain orientations distribute randomly. The histogram of grain size distribution in Fig. 4b shows that the grain size is mostly around 15 nm. After LSP with the energy of 7J, as the laser pulse energy increase, the dislocation density of the hardened layer rises, the grain is further refined with the size of about 10 nm, and the corresponding SAED pattern is more continuous and clearer (see Fig. 4c and 4d). Moreover, after LSP, the surface structure of the local area is amorphized as given by Fig. 4e and 4f. The corresponding SAED patterns show halos, which confirms the existence of the amorphous phase. The degree of amorphization increases with the pulse energy. Similar phenomenon was found in Luo's results [25]. It was stated that the liquid-solid mixed structure caused by local temperature rising and subsequent rapid cooling was the main reason for the formation of such an amorphous phase. Also, Ye et al. [26] found that an amorphous phase was produced in the NiTi alloy after LSP. High work hardening on the sample surface introduced by plastic deformation at ultra-high strain rate results in the amorphization. The amorphous phases enhance the mechanical properties of the material.

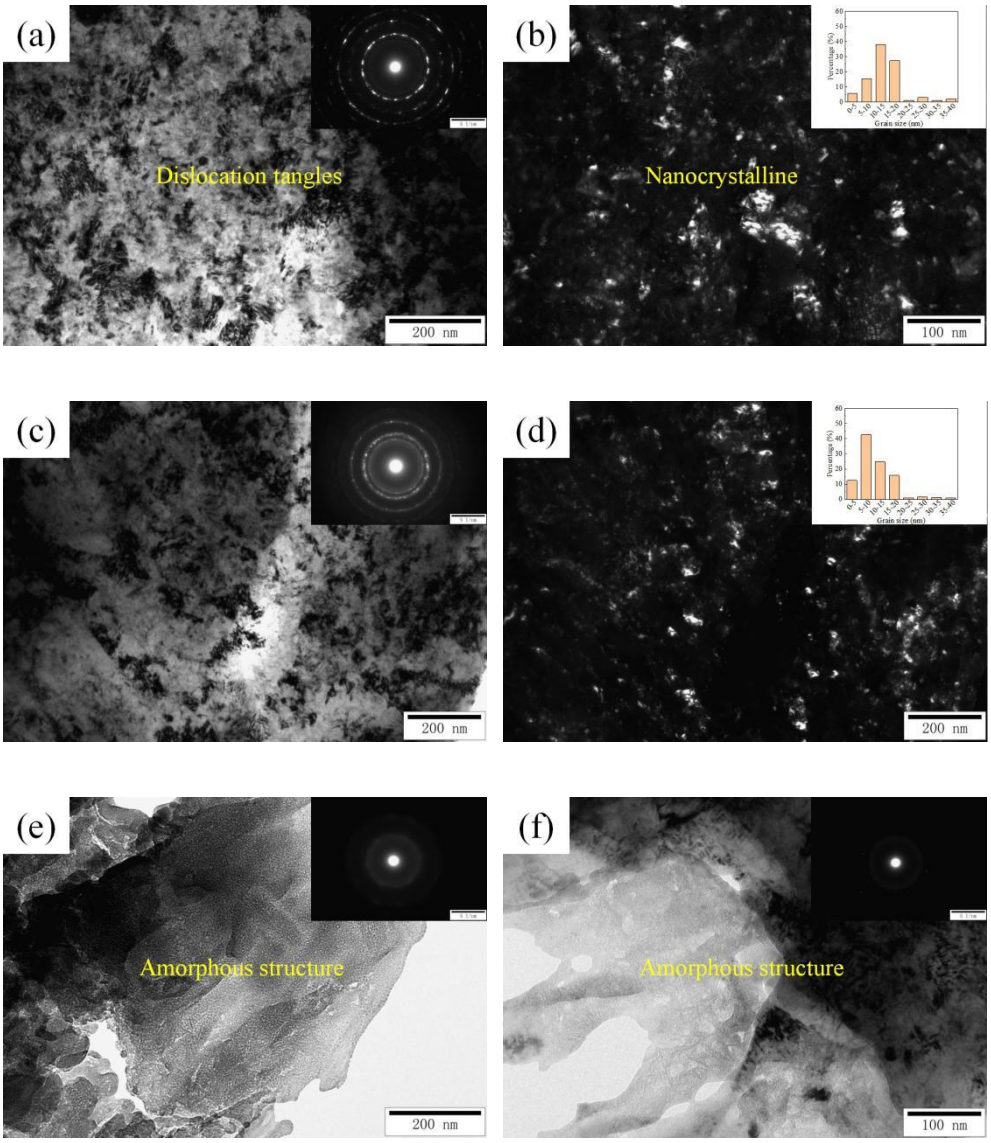

Fig. 4 TEM images of the 300M steel surfaces subjected to LSP with different pulse energies: (a, b, e) LSP-3J; (c, d, f) LSP-7J.

Fig. 5 shows TEM images of subsurface layers (100 μm below the surface) of the 300M steel after LSP with different laser pulse energies. Due to the absorption of the plasma-induced shock wave by the surface layer of 300M steel, the impact energy received by the subsurface layer was significantly reduced. After LSP with a low laser pulse energy of 3J, the needle-like tempered martensite is broken, and the effect of grain refinement is small (Fig. 5a). High density dislocation lines were developed in the grains of subsurface layer during the plastic deformation. The dislocation lines piled up and contributed to the formation of dislocation tangles and dense dislocation

walls (Fig. 5b). Due to the high energy shock wave, the dislocation density in the subsurface layer of LSP-7J sample increases and a large amount of deformation twins (DTs) are formed as seen in Fig. 5c and 5d. Compared with the surface layer of the sample, the degree of the grain refinement of the subsurface layer of 300M steel reduces. The microstructure of 300M steel changes from nano-crystalline and local amorphous structures (surface layer) to substructure defects such as dislocation tangles and mechanical twins (subsurface layer), and then to the dislocation lines (in the core). This is mainly because the strain and strain rate gradually decrease with the depth of the deformation layer during LSP treatment [27].

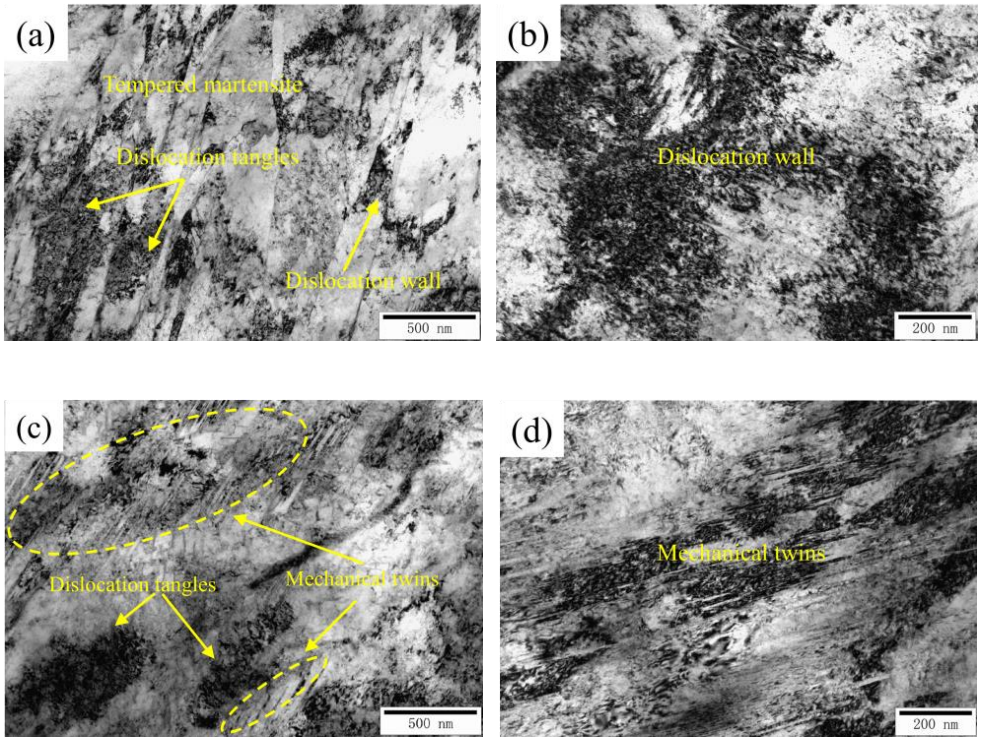

Fig. 5 TEM images of the subsurface 300M steel at 100 μm below surface subjected to LSP with different pulse energies: (a, b) LSP-3J; (c, d) LSP-7J.

3.3 XRD analysis

Fig. 6 shows the XRD patterns for 300M steel after LSP treatments with different pulse energies. In Fig. 6a, three diffraction peaks of (110), (200) and (211)

reflections are still retained and there is no additional diffraction peak, indicating no new phase formation within 300M steel during LSP. The full widths at half maximum (FWHM) of (110) reflections are increased from 0.386° (without LSP) to 0.478° (LSP-3J) and 0.483° (LSP-7J) following the increase of the incident laser power. This can be attributed to grain refinement of the surface structure. Similar phenomenon was also observed in TC11 [25] and TC6 [28] titanium alloys treated via LSP method. Further, diffraction peaks of the samples after LSP shifted to smaller diffraction angles (Fig. 6b), which was ascribed to change in the grain refinement and microstrain of 300M steel after LSP. The average grain size and microstrain of the sample surface can be evaluated by using the Williamson-Hall (W-H) method [29], [30],

$$\beta \cos\theta = \varepsilon(4 \sin\theta) + K\lambda/D \tag{1}$$

The formula (1) has a linear relationship similar to Y=mX+c. Therein, $\beta \cos\theta$ is Y, (4 $\sin\theta$) X, and $K\lambda/D$ intercept of Y. More specifically, β is the FWHM of the diffraction peak, K the constant ~0.9, λ the wavelength of 0.154056 nm (Cu Kα source), D the average grain size, θ the Bragg diffraction angle (in radians), and ε the microstrain. Following the formula, surface microstrains were calculated to 0.22% and 0.28%, respectively, and average grain sizes are 12.8 nm and 10.7 nm, as shown in Fig. 6c. In addition, the value of the dislocation density ρ is calculated from the average grain size D and microstrain $\langle\varepsilon^2\rangle^{1/2}$ from the following equation [31]

$$\rho = \frac{3\sqrt{2\pi}\langle\varepsilon^2\rangle^{1/2}}{Db} \tag{2}$$

where b is the Burgers vector ($b = \frac{\sqrt{3}a}{2}$ for the BCC structure where a is the lattice parameter).

Evaluated by equation (2), the dislocation density of the sample after LSP with the pulse energy of 3J and 7J are found to be 5.249×10^{14} and 7.962×10^{14} 1/m^2. With the increase of laser pulse energy, the microstrain and dislocation density increase,

while the grain size decreases. The trends are consistent with the result of the microstructure evolution (Fig. 4).

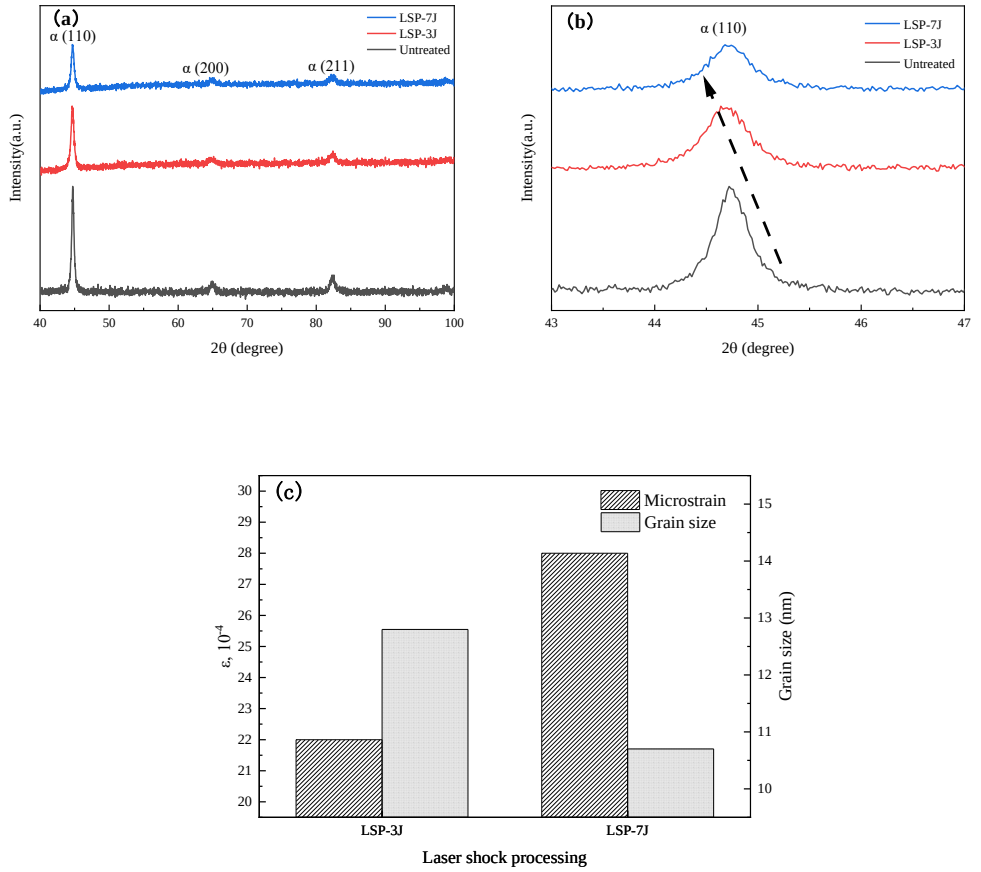

Fig. 6 X-ray diffraction patterns of 300M steel subjected to LSP with different pulse energies.

3.4 Mechanical properties

3.4.1 Residual stress analysis

Residual stress profiles in depth direction are plotted in Fig. 7 for the 300M steel treated with LSP of different pulse energies. The untreated regions are in a small stress state (10 MPa) due to the machining effect. It should be noted that the residual stress increases with the pulse energy. After 3J LSP , the maximum residual stress is -422 MPa and the corresponding depth of compressive residual stress is 160 μm. The laser owns a high power density (GW/cm^2) and short pulse (10-30 ns). It passes

through the transparent confinement layer and acts on the absorption coating. The coating fully absorbs the laser energy and can be quickly vaporized to form plasma. The plasma absorbs the laser energy, expands rapidly, and acts on the surface of the material in the form of a shock wave at an ultra-high strain rate. The surface is then severely plastically deformed. When the peak pressure of the shock wave induced by the high-pulse energy, laser exceeds the dynamic yield strength of the material, and a large number of dislocations are produced and the strain hardening occurs, which further led to a certain thickness of compressive residual stress layer on the surface of the material [32]. As per report, the compressive residual stress near the surface of the sample is caused by local plastic deformation after LSP. Also, a higher pulse energy leads to a larger deformation. Therefore, the value of residual stress and the depth of the affected layer increase with the increase in laser pulse energy. The maximum residual stress of the sample after LSP with the laser pulse energy of 7J is -564 MPa and the corresponding depth 200 μm. Furthermore, the maximum compressive residual stress is generated by the LSP impact in the surface layer. Ref. [33] reported that the maximum compressive residual stress of the 300M steel after SP stayed on the subsurface layer. The similar phenomenon was also observed in titanium alloy [34], [35] and Fe-0.8%C high carbon steel [36]. This is mainly due to the heat effect of the surface of the material after SP. However, LSP is used as a cold-worked surface strengthening process. As the effect of the absorption layer, the surface of the sample is protected from the thermal effect, so the maximum compressive residual stress appears on the surface layer.

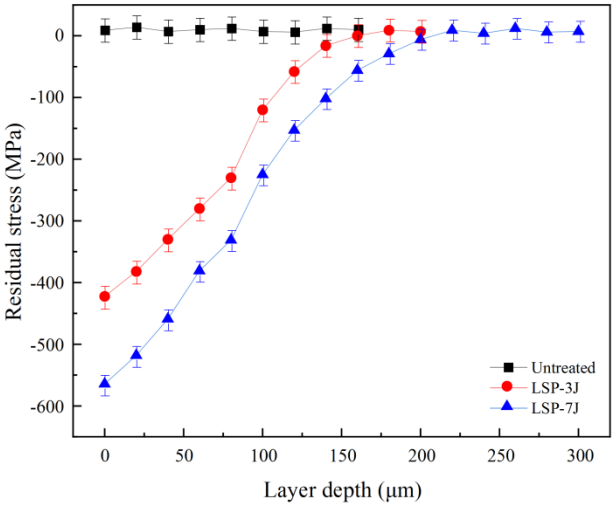

Fig. 7 Residual stress of 300M steel subjected to LSP with different pulse energies at different layer depths.

3.4.2 Nano-indentation hardness analysis

Fig. 8 shows the nano-indentation hardness profiles of the 300M steel after LSP with different pulse energies in depth direction. As visible, the hardness of the untreated sample has no significant change from the surface to the center with the value of about 11.2 GPa. After LSP with the laser pulse energy of 3J, the surface hardness of the 300M steel increases significantly and the hardness is about 18.3 GPa, which is 63.4% higher than that of the untreated sample. The depth of the hardened area reaches to about 100 μm. Further, as the laser pulse energy increases to 7J, the surface hardness of the sample reaches to about 19.1 GPa, which is again 70.5% higher than that of the untreated sample. The depth of the hardened area is near 140 μm. Due to the severe plastic deformation of 300M steel surface induced by high-energy shock waves, the density of sub-structure defects greatly increases, which results the accumulation of a large number of dislocations and hinders the movement of dislocations, resulting in observed work hardening of the material. Meanwhile, the grains of 300M steel are refined due to high-energy shock waves and the surface structure of the local area is amorphized. Under the combined action of work hardening and grain refinement, the surface hardness of 300M steel is significantly

improved. Rai et al. [37] stated that the generation, annihilation and recombination of high-density dislocations as well as the grain refinement of the 9Cr-1Mo steel after LSP cause the increase of the surface hardness. With the increase in the distance to the treated surface, the corresponding nanoindentation hardness gradually decreases [38]. LSP induces a high-pressure plasma shock wave on the surface of 300M steel, but the shock wave energy gradually attenuates during the propagation process in the material, leading to the reduced degree of the plastic deformation and increased grain size. Further, the effects of work hardening and grain refinement are weakened. Thus, the hardness presents a gradient change characteristic. This observation is also consistent with the change in the microstructure.

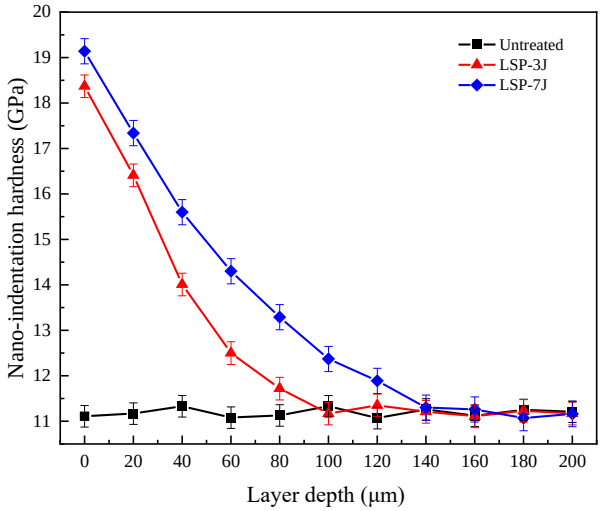

Fig. 8 Nano-indentation hardness of 300M steel subjected to LSP with different pulse energies at different layer depths.

3.4.3 Tensile properties analysis

Tensile properties were plotted in Fig. 9 for 300M steel after LSP with different laser pulse energies. The yield strength and ultimate tensile strength of the untreated sample are 1511 and 1815 MPa, respectively, and the elongation is 11.8%. The strength and plasticity of 300M steel increase with the laser pulse energy applied during LSP. The yield strength increases 9.93% to 1661 MPa, ultimate tensile strength

6.45% to 1932 MPa, and the elongation increases 8.47% to a value of 12.8%. The presence of compressive residual stresses induced by LSP will have a beneficial effect on the fatigue performance. It is well known that fatigue cracks mostly originate at the surface of materials, while a compressed surface layer will inhibit the crack initiation and growth, which prolongs the crack propagation life [32]. After LSP, a gradient structure is formed from the sample surface to the center. The observed surface layer is within nanometer scale. The coarse-grained structure in the center shows good plastic deformation ability. Due to high tensile strain and work hardening ability, the strain concentration and early necking can be suppressed, which delays the deformation localization and crack initiation of the surface nanocrystalline structure [39]. This results in the gradient nanostructure with good tensile plastic deformation ability. Under the combined action of these factors, the strength and plasticity of 300M ultra-high-strength steel are improved after LSP.

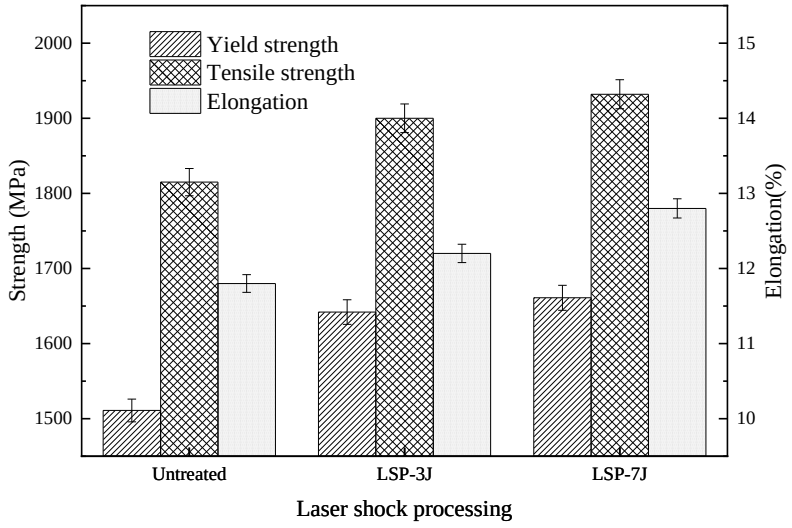

Fig. 9 Tensile properties of 300M steel subjected to LSP with different pulse energies.

3.4.4 Tensile fracture morphology

The fracture surface morphologies of the 300M steel after LSP with different laser pulse energies are shown in Fig. 10. The untreated sample has the ductile fracture given by Fig. 10a. A large number of small and shallow dimples show

uniform distribution with an average size is about 1 μm. After LSP, the fracture morphology shows a mixture of quasi-cleavage and ductile fracture. The quasi-cleavage fracture occurs in the SPD layer at the sample surface with the depth of ~ 10 μm. As the laser pulse energy increases, the depth of the SPD layer increases to ~ 20 μm. The fracture morphology of the SPD layer is different from the corresponding matrix morphology, and a large area of cleavage surface appears, showing typical quasi-cleavage fracture characteristics (Fig. 10b and 10c). This observation is consistent with the result of LY2 alloy after multiple LSP by Lu et al. [40]. Due to high-energy shock wave, the grain size of the SPD layer of the 300M steel is significantly refined to the nanoscale (Fig. 4b and 4d). Meanwhile, the dislocation density increases, and the dislocation tangles have been transformed into dislocation walls (Fig. 4a and 4c), which prevents the plastic deformation, resulting the surface fracture morphology to quasi-cleavage fracture. Surface nano crystallization has been found as the main factor in the transformation of the fracture morphology of the 300M steel after LSP, which improves the strength and plasticity of the 300M steel (Fig. 9).

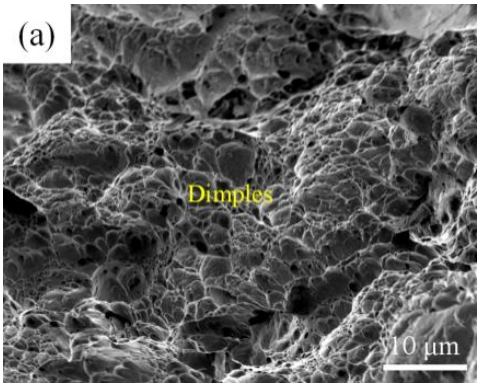

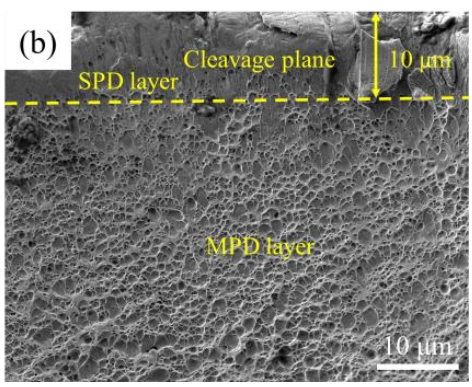

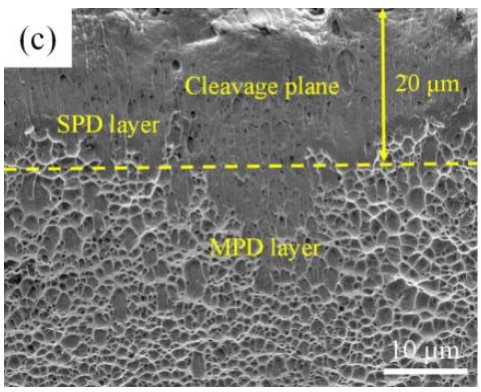

Fig. 10 Tensile fracture morphology of 300M steel subjected to LSP with different pulse energies: (a) untreated; (b) LSP-3J; (c) LSP-7J.

4. Discussion

The surface GNs of 300M steel is created by LSP treatment to substantially enhance mechanical properties. After an LSP treatment, the GNs of 300M steel will have an SPD layer, MPD layer and the core matrix structure (Fig. 3). Under the action of high-energy shock waves, the surface of 300M steel undergoes severe plastic deformation and forms high-density dislocations. Dislocation rearrangements produce a large number of dislocation cells. Due to the dynamic recovery, the dislocation cell further evolves into SGBs. With the continuous movement of dislocations, SGBs gradually transform into HAGBs [41], and thus the grains are refined to the nanoscale.

Furthermore, the grain of 300M steel is amorphized after LSP treatment, as shown in Fig. 4e and 4f. Amorphization is generally regarded as an extreme case of the grain refinement. When this occurs, the process of grain nano crystallization has also passed its tipping point. The grains are so small that it's difficult to clearly define the grain boundaries. Therefore, the amorphization of the grains during the deformation requires a higher impact pressure. When the free energy of the grains is higher than that of the amorphous phase, the grain is amorphized [26]. According to the Fabbro model [42], the peak pressure induced by laser is evaluated as follows:

$$P_{max}(\mathrm{GPa}) = 0.01\sqrt{\frac{\alpha}{2\alpha+3}}\sqrt{Z(g\ cm^{-2}s^{-1})}\sqrt{I_0(\mathrm{GW}\ cm^{-2})} \quad (3)$$

Here, α is the ratio of thermal energy to the internal energy of the plasma (usually $\alpha \approx 0.25$); Z ($\frac{2}{Z} = \frac{1}{Z_1} + \frac{1}{Z_2}$) is the acoustic impedance, Z_1 is the target acoustic impedance (Z_1=4.54 × 10^6 g $cm^{-2}s^{-1}$), Z_2 is the acoustic impedance of the water confinement layer (Z_2=1.65 × 10^5g $cm^{-2}s^{-1}$); I_0 ($I_0 = \frac{4E}{\pi d^2 \tau}$) is the laser energy

density, E is the pulse energy (J), d is the diameter of laser spot (cm), and τ is the pulse width (s).

Evaluated by equation (3), when E are 3 and 7J, P_{max} are approximately 2.2 and 4.5 GPa, respectively. Besides, according to the Hugoniot elastic limit (HEL) model [43], the σ_{HEL} of 300M steel is about 2.0 GPa, as shown in formula (4):

$$\sigma_{HEL} = \sigma_Y^D \frac{1-v}{1-2v} \tag{4}$$

Here, σ_Y^D is the dynamic yield strength, and v is the Poisson's ratio of 300M steel (v≈0.2).

During LSP treatment, when the peak pressure of the shock wave is higher than the HEL of 300M steel, the plastic deformation with ultra-high strain rate occurs on the surface of the material, resulting in the accumulation of defects (such as high-density dislocations and twins) and atomic disordering in materials. Due to the increase in the free energy of the system, the free energy of the grains is higher than the critical value of amorphization. Thus, the amorphous phase is formed on the surface of 300M steel. With the increase in laser pulse energy, the peak pressure of the shock wave increases significantly to a value far exceeding the 2HEL of 300M steel. The strain rate of the surface sample rises and the free energy of the crystalline phase increases, which promotes the amorphous transformation of surface grains.

With the depth of layer increases, the DTs form on subsurface layer of 300M steel to coordinate the plastic deformation. The grains within the subsurface layer are refined under the interaction of twins and dislocations (Fig. 5). The formation of DTs depends on the SFE of the material. The spacing of the slip plane of the material with a low SFE is relatively large. At a high strain rate, it is difficult for dislocations to slip and the stress concentration occurs, which results in the formation of the DTs to coordinate the deformation [44]. For the materials with a higher SFE, more energy and stress are required to form twins. Therefore, the formation of DTs of 300M steel after LSP may be attributed to the high density of dislocations, stress concentration,

shock waves and local high energy and strain caused by nanocrystals (Fig. 5a and 5c). After LSP with the laser pulse energy of 3J, the strain rate of 300M steel on the subsurface layer is low, and only a small amount of deformation twins is formed (Fig. 5b). As the pulse energy rises, the strain rate and the dislocation density increase sharply, leading to the increase of the amounts of the DTs. This is mainly related to the different strain rate of the 300M steel on the subsurface after LSP with different pulse energy. This effect can be assessed by Zener-Hollomon parameters [45]:

$$\ln Z = \ln \dot{\varepsilon} + \frac{Q'}{RT} \quad (5)$$

where, $\dot{\varepsilon}$ is the strain rate, Q' is the activation energy of atomic diffusion, R is the gas constant, and T is the deformation temperature.

Equation (5) indicates that the ln Z rises with the increase in the strain rate of the 300M steel on the subsurface, which is equivalent to the decrease of the SFE of materials [46]. The critical stress for the formation of the twinning reduces and the dislocation slipping is hindered, which leads to the increase of the internal stress and the aggravation of the stress concentration. The internal stress generated by the dislocation pile-up is more likely to attend the critical twin stress and the amount of DTs increases significantly. Therefore, the degree of grain refinement of the 300M steel on the subsurface increases. From the above it can be found that the dislocation movement remains as the main mechanism of surface nano-crystallization of 300M steel after LSP treatment, while the DTs on the subsurface coordinate and promote the grain refinement. Similar phenomenon was also observed in the precipitation hardening stainless steel after USRP by Liu et al. [47].

The laser pulse energy has a significant effect on the microstructure and mechanical properties of the gradient nanostructure of 300M steel. The residual compressive stress (Fig. 7) and the hardness (Fig. 8) of 300M steel rises significantly as the increase of the laser pulse energy. The strength and plasticity of 300M steel are also improved (Fig. 9). Theoretically, the strength and hardness of the materials can be evaluated by formula (6) [47]:

$$\sigma_f = \sigma_0 + k(d_{fp})^{-1/2} + \alpha G b \rho^{1/2} \quad (6)$$

In the formula,σ_f is the strength, σ_0 is the friction stress, k is the Hall-Petch constant, d_{fp} is the mean free path of the dislocation, G is the shear modulus, b is the Berth vector and ρ is the dislocation density.

Equation (6) suggests that the strength or hardness of the material rises with the increase of the dislocation density and the decrease of the mean free path of dislocations. During LSP treatment, the peak pressure of the shock wave (P_{max}) rises significantly as the pulse energy increases. The plastic deformation on the surface of 300M steel aggravates (Fig. 3) and the dislocation density increases sharply (Equation (2)). The grains are significantly refined, and more grains become amorphous (Fig. 4e and 4f). As a result, the mean free path of dislocations reduces and the hardness of 300M steel is significantly improved. In addition, after LSP treatment the DTs are formed on the subsurface of the 300M steel. The d_{fp} reduces under the interaction of dislocations and twin boundaries, and the strength of the material rises. The influence of the grain boundary and twin boundary on d_{fp} can be described as follows [48]:

$$\frac{1}{d_{fp}} = \frac{1}{d_{twin}} + \frac{1}{d_{sub}} \quad (7)$$

Here d_{twin} and d_{sub} are the spacing of the twin boundaries and sub-grain boundaries, respectively. From equation (7), with the increase in laser pulse energy, the number of DTs and the density of the twin boundary on the subsurface of 300M steel increases significantly (Fig. 5). The mean free path of dislocations (d_{fp}) is reduced by the interaction of dislocations and twins. As a result, the strength of the material increases.

5. Conclusion

The GNs were introduced on the surface of 300M steel by LSP treatment. The resulted microstructure evolution and properties of GNs induced by LSP with

different pulse energy of in UHS 300M steel were studied systematically. Following conclusions have been drawn with this study:

(1) After LSP treatment, the surface grains of 300M steel have been remarkably refined and some of the grains become amorphized. Many substructure defects such as dislocation tangles and deformation twins turned out on the subsurface of the materials. With the increase of laser pulse energy, the degree of the grain refinement rises and the amorphization becomes more obvious. The dislocation density of the subsurface materials and the number of deformation twins also rises.

(2) The depth of the GNs of 300M steel increases significantly following the pulse laser energy. The surface hardness and residual stress of 300M steel are significantly enhanced. The corresponding strength and plasticity are improved too.

(3) The fracture morphology of the 300M steel changes from typical ductile fracture before LSP to mixed of quasi-cleavage and ductile fracture after LSP.

Acknowledgment

This work was supported by the National Natural Science Foundation of China [grant numbers U1804146, 52111530068 and 51905153]; the Science and Technology Innovation Team of Henan University of Science and Technology [grant number 2015XTD006]; the Foreign Experts Introduction Project of Henan Province [grant number HNGD2020009]; and the Academy of Finland [grant number 311934].

References

[1] S. S. Zhang, M. Q. Li, Y. G. Liu, J. Luo, T. Q. Liu. *Mater. Sci. Eng. A.* **2011**, 528(15), 4967-4972.

[2] F. Liu, X. Lin, H. Yang, X. Wen, Q. Li, F. Liu, W. Huang. *Mater. Sci. Eng. A.* **2017**, 695, 258-264.

[3] Q. Guo, J. H. Liu, M. Yu, S. M. Li. *Acta Metall. Sin. (Engl. Lett.).* **2014**, 28(2), 139-146.

[4] A. Hameed, O. Zubair, T. S. Ali, Z. Mehmood, A. Javed, Z. Mehmood. *Eng. Fail. Anal.* **2020**, 117, 104847.

[5] P. Skubisz, J. Sinczak. *Aircr. Eng. Aerosp. Technol*. **2018**, 90(5), 713-719.

[6] A. Bag, M. Levesque, M. Brochu. *Int. J. Fatigue*. **2020**, 131, 105346.

[7] W. Zhao, D. Liu, X. Zhang, Y. Zhou, R. Zhang, H. Zhang, C. Ye. *Int. J. Fatigue*. **2018**, 121, 30-38.

[8] W. Zhao, D. Liu, X. Zhang, H. Zhang, J. Liu, C. Ma, R. Zhang, Y. Dong, C. Ye. *Surf. Coat. Technol.* **2020**, 397, 125994.

[9] W. Zhao, D. Liu, J. Liu, X. Zhang, H. Zhang, R. Zhang, Y. Dong C. Ye. *Adv. Eng. Mater.* **2020**, 23 (3), 2001203.

[10] E. Gürses, T. El Sayed. *Mater. Lett.* **2011,** 65, 3391-3395.

[11] N. R. Tao, J. Lu, K. Lu. *Mater. Sci. Forum*. **2008**, 579, 91-108.

[12] S. Bahl, S. Suwas, T. Ungàrb, K. Chatterjeea. *Acta Mater*. **2017**, 122, 138-151.

[13] H. W. Zhang, Z. K. Hei, G. Liu, J. Lu, K. Lu. *Acta Mater*. **2003**, 51(7), 1871-1881.

[14] K. Y. Zhu, A. Vassel, F. Brisset, K. Lu, J. Lu. *Acta Mater*. **2004**, 52(14), 4101-4110.

[15] W. Guo, R. Sun, B. Song, Y. Zhu, F. Li, Z. Che, B. Li, C. Guo, L. Liu, P. Peng. *Surf. Coat. Technol.* **2018**, 349, 503-510.

[16] A. Chattopadhyay, G. Muvvala, S. Sarkar, V. Racherla, A. K. Nath. *Opt. Laser Technol.* **2021**, 133, 106527.

[17] S. Lou, Y. Li, L. Zhou, X. Nie, G. He, W. He. *Mater. Des.* **2016**, 104(15), 320-326.

[18] Y. H. Wu, *Adv. Mater. Res.* **2013**, 2856, 1122-1126.

[19] T. E. Pistochini, M. R. Hill. *Fatigue Fract. Eng. Mater. Struct.* **2011**, 34(7), 521-533.

[20] Z. W. Cao, S. L. Gong, Y. Gao. *Adv. Mater. Res*. **2013**, 2262, 2378-2383.

[21] Y. K. Zhang, J. Z. Lu, X. D. Ren, H. B. Yao, H. X. Yao. *Mater. Des.* **2009**, 30(5), 1697-1703.

[22] C. Wang, K. Luo, X. Bu, Y. Su, J. Cai, Q. Zhang, J. Lu. *Corros. Sci.* **2020**, 177, 109027.

[23] J. Z. Lu, K. Y. Luo, Y. K. Zhang, G. F. Sun, Y. Y. Gu, J. Z. Zhou, X. D. Ren, X. C. Zhang, L. F. Zhang, K. M. Chen, C. Y. Cui, Y. F. Jiang, A. X. Feng, L. Zhang. *Acta Mater.* **2010**, 58(16), 5354-5362.

[24] X. Y. Mao, J. Y. Sun, Y. Y. Feng, X. M. Zhou, X. M. Zhao. *Mater. Lett.* **2019**, 246, 178-181.

[25] S. Luo, L. Zhou, X. Wang, X. Cao, X. Nie, W. He. *Mater.* **2018**, 11(4), 563.

[26] Y. Chang, S. Suslov, X. Fei, G. J. Cheng. *Acta Mater.* **2011**, 59(19), 7219-7227.

[27] J. Z. Lu, K. Y. Luo, Y. K. Zhang, C. Y. Cui, G. F. Sun, J. Z. Zhou, L. Zhang, J. You, K. M. Chen, J. W. Zhong. *Acta Mater.* **2010**, 58(11), 3984-3994.

[28] L. Zhou, Y. Li, W. He, G. He, X. Nie, D. Chen, Z. Lai, Z. An. *Mater. Sci. Eng. A*. **2013**, 578, 181-186.

[29] S. Brandstetter, P. M. Derlet, P. S. Van, H. S. Van. *Acta Mater.* **2008**, 56(2), 165-176.

[30] J. Markmann, V. Yamakov, J. Weissmüller. *Scr. Mater.* **2008**, 59(1), 15-18.

[31] G. Dini, R. Ueji, A. Najafizadeh, S. M. Monir-Vaghefi. *Mater. Sci. Eng. A*. **2010**, 527(10), 2759-2763.

[32] Y. Xiong, P. Li, L. Chen, Y. Lu, J. Wang, F. Ren. *Chin. J. Mater. Res.* **2015**, 29(6),

469-474.

[33] G. Lu, F. Lu. *Mater. Mech. Eng. (China).* **2015**, 39(01), 20-23+28.

[34] J. Lindemann, C. Buque, F. Appel. *Acta Mater.* **2006**, 54(4), 1155-1164.

[35] E. Maawad, Y. Sano, L. Wagner, H. G. Brokmeier, C. Genzel. *Mater. Sci. Eng. A*. **2012**, 536, 82-91.

[36] Y. Xiong, T. He, P. Li, L. Chen, F. Ren, A. A. Volinsky. *J. Cent. South Univ.* **2015**, 22(12), 4515-4520.

[37] A. K. Rai, R. Biswal, R. K. Gupta, R. Singh, S. K. Rai, K. Ranganathan, P. Ganesh, R. Kaul, K. S. Bindra. *Surf. Coat. Technol*. **2019**, 358, 125-135.

[38] X. Y. Mao, J. Y. Sun, X. M. Zhou, W. W. Sun, X. M. Zhao. *J. Mater. Eng. Perform*. **2020**, 29, 6952-6959.

[39] K. Lu. *Acta metall. sin. (China).* **2015**, 51(1):1-10.

[40] J. Z. Lu, K. Y. Luo, Y. K. Zhang, J. Z. Zhou, X. G. Cui, L. Zhang, J. W. Zhong. *Mater. Sci. Eng. A.* **2010**, 528(2), 730-735.

[41] T. Zhou, Y. Xiong, Z. G. Chen, X. Q. Zha, Y. Lu, T. T. He, F. Z. Ren, H. Singh, J. Kömi, M. Huttula, W. Cao. *Surf. Coat. Technol.* **2021**, 421, 15.

[42] R. Fabbro, J. Fournier, P. Ballard, D. Devaux, J. Virmont. *J. Appl. Phys.* **1990**, 68(2), 775-784.

[43] J. N. Johnson, R. W. Rohde. *J. Appl. Phys*. **1971**, 42(11), 4171-4182.

[44] Y. Gao, X. Tao, *Explosion Shock Waves.* **2021**, 41(04), 4-29.

[45] X. H. An, S. D. Wu, Z. G. Wang, Z. F. Zhang. *Prog. Mater. Sci.* **2019**, 101, 1-45.

[46] Y. S. Li, Y. Zhang, N. R. Tao, K. Lu, *Acta Mater.* **2009**, 57(3), 761-772.

[47] D. Liu, D. Liu, X. Zhang, C. Liu, N. Ao. *Mater. Sci. Eng. A.* **2018**, 726, 69-81.

[48] C. Ye, A. Telang, A. S. Gill, S. Suslov, Y. Idell, K. Zweiacker, J. M. K.

Wiezorek, Z. Zhou, D. Qian, S. R. Mannava, V. K. Vasudevan. *Mater. Sci. Eng. A*. 2014, 613 274-288.